

Article

Development of a Diagnostic Algorithm for Detecting Freezing Precipitation from ERA5 Dataset: An Adjustment to the Far East

Mikhail Pichugin , Irina Gurvich , Anastasiya Baranyuk , Vladimir Kuleshov  and Elena Khazanova 

Far Eastern Branch, V.I. Il'ichev Pacific Oceanological Institute, Russian Academy of Sciences, 43, Baltiyskaya, 690041 Vladivostok, Russia; gurvich@poi.dvo.ru (I.G.); vykochko@poi.dvo.ru (A.B.); khazanova@poi.dvo.ru (E.K.)

* Correspondence: pichugin@poi.dvo.ru

Abstract: Freezing precipitation and the resultant ice glaze can have catastrophic impacts on urban infrastructure, the environment, forests, and various industries, including transportation, energy, and agriculture. In this study, we develop and evaluate regional algorithms for detecting freezing precipitations in the Far East, utilizing the ERA5 reanalysis dataset from the European Centre for Medium-Range Weather Forecasts, along with standard meteorological observations for 20 cold seasons (September–May) from 2004 to 2024. We propose modified diagnostic algorithms based on vertical atmospheric temperature and humidity profiles, as well as near-surface characteristics. Additionally, we apply a majority voting ensemble (MVE) technique to integrate outputs from multiple algorithms, thereby enhancing classification accuracy. Evaluation of detection skills shows significant improvements over the original method developed at the Finnish Meteorological Institute and the ERA5 precipitation-type product. The MVE-based method demonstrates optimal verification statistics. Furthermore, the modified algorithms validly reproduce the spatially averaged inter-annual variability of freezing precipitation activity in both continental (mean correlation of 0.93) and island (correlation of 0.54) regions. Overall, our findings offer a more effective and valuable tool for operational activities and climatological assessments in the Far East.

Keywords: freezing rain; extreme weather; ERA5 reanalysis; meteorological observations; diagnostic algorithm; Far East



Citation: Pichugin, M.; Gurvich, I.; Baranyuk, A.; Kuleshov, V.; Khazanova, E. Development of a Diagnostic Algorithm for Detecting Freezing Precipitation from ERA5 Dataset: An Adjustment to the Far East. *Climate* **2024**, *12*, 224. <https://doi.org/10.3390/cli12120224>

Academic Editors: Helena A. Flocas and Charles Jones

Received: 28 October 2024
Revised: 5 December 2024
Accepted: 14 December 2024
Published: 17 December 2024



Copyright: © 2024 by the authors. Licensee MDPI, Basel, Switzerland. This article is an open access article distributed under the terms and conditions of the Creative Commons Attribution (CC BY) license (<https://creativecommons.org/licenses/by/4.0/>).

1. Introduction

Freezing precipitation (FZRA)—which occurs as rain or drizzle—typically forms in the warm atmospheric front zones due to advective temperature inversion in the lower troposphere. This process involves a warm and moist air mass with positive temperatures flowing over a colder near-surface layer with temperatures below or near 0 °C [1]. As solid precipitation falls, it partially or completely melts in the elevated warm layer, transforming into rain through the “melting process”. In the cold layer, the raindrops become supercooled and upon contact with exposed objects, and they form a dense, smooth, transparent ice known in meteorology as glaze ice. At high cloud top temperatures, FZRA can begin as liquid precipitation (“warm rain”), with raindrops becoming supercooled in the cold near-surface air, leading to the formation of an icy crust on surfaces [2–7]. The glaze ice phenomena associated with FZRA can have catastrophic impacts on urban infrastructure, the environment, the economy, and human health [8–10]. According to the American Meteorological Society Glossary of Meteorology, intense and prolonged FZRAs with glaze ice measurements of 6 mm or more in diameter are classified as ice storms.

The most destructive impacts of FZRA are observed in North America, Canada, and Europe, including European Russia [8,11–14]. In the Far East, intense and prolonged freezing precipitation occurs less frequently and tends to cause less damage. However, from September to May, freezing precipitation of varying intensity and duration is recorded

in the different Far East areas, mainly driven by southern synoptic processes. Notable examples of destructive FZRA include the events of 18–19 November 2020, in the southern part of Primorsky Krai [10,14,15], 1–3 January 2011 in Guizhou Province, China [16], and 3 January 2003 over Kanto Plain, Japan [4]. The regional features of terrain topography significantly influence the intensity and duration of FZRA [17,18], which is likely one of the reasons for the pronounced geographical heterogeneity in their localization. Another probable reason is the temporal heterogeneity of the observations (see Section 3.1).

Research on FZRA in the Far East encompasses a range of topics, including formation mechanisms and synoptic conditions [4,14–20], as well as the development of climatology and forecast models [5,21–23]. However, it is important to note that these studies have been confined to specific areas, such as South Korea, Japan, China, and the Russian Far East. Comprehensive climate studies covering the entire Far Eastern region are lacking, with the exception of global distribution analyses of FZRA [7].

A series of studies have investigated the synoptic conditions, formation mechanisms, and climatic characteristics of FZRA, primarily utilizing meteorological observations and upper air soundings [11,24–26]. A notable limitation of this approach is the spatial heterogeneity inherent in the standard meteorological observation network, which can compromise the reliability of the derived statistical estimates and climatic characteristics. The use of reanalysis and modeling techniques offers a solution by addressing gaps in datasets caused by the uneven spatial distribution of meteorological observations [6,7,12,13,27–29]. An increasingly pertinent research area involves forecasting the variability in the frequency of FZRA events and the shift in their predominant localization due to global warming [13,30,31].

The primary limitation of reanalysis-based predictive and climate models lies in the significant errors associated with the algorithms used to diagnose freezing precipitation. As demonstrated by Reeves et al. [32] and Kmarainen et al. [28], even minor deviations in the vertical temperature distribution can influence the type of precipitation. Furthermore, the mismatch between the horizontal resolution of the reanalysis data and the scale of FZRA events may lead to a discrepancy between the predicted temperatures in the melting and freezing layers with the actual thresholds at which these layers form. Consequently, the reliability of FZRA identification by most algorithms is compromised due to the inadequate horizontal, vertical, and temporal resolution of the reanalysis data.

Detecting freezing precipitation and accurately distinguishing it from ice pellets is a complex task, being particularly challenging in regions with significant terrain heterogeneity. Two primary approaches are used to identify precipitation types: (1) the implicit (diagnostic) approach, which utilizes vertical profiles of temperature, humidity, and geopotential height [33–37] to predict the expected precipitation phase on the surface; and (2) the explicit approach, which is based on microphysics models [38–40] that describe the characteristics of hydrometeors and account for their interactions. The explicit approach, grounded in physical principles, offers the potential for higher accuracy but demands significant computational resources. Although diagnostic algorithms are used more frequently in climatological studies, comparative analyses [41] have revealed substantial differences in determining the type of precipitation, with diagnostic methods showing limited capability in identifying FZRA compared to snow or rain [32].

FZRA, which includes freezing rain and drizzle, is often accompanied by snow or ice pellets. The effectiveness of existing algorithms is often compromised by their inability to accurately distinguish between these forms of precipitation [32]. Algorithms designed to diagnose mixed precipitation, which includes combinations of freezing rain/drizzle and ice pellets, have demonstrated significantly improved performance [31]. Nonetheless, FZRA remains the primary glaze-forming factor, leading to severe impacts on infrastructure and populations. This underscores the need to develop algorithms with advanced capabilities to accurately identify FZRA events.

This study aims to develop and validate a regional FZRA detection algorithm using the high-resolution ERA5 reanalysis dataset and standard meteorological measurements over 20 cold seasons (September–May) from 2004 to 2024. The study area is defined by the

coordinates 25–65° N and 10–150° E, which have been selected based on climatic conditions and typical synoptic processes that contribute to the formation of freezing precipitation in the Far Eastern region.

Section 2 provides a description of the meteorological observation and ERA5 reanalysis datasets used in this study, as well as the methods applied. Section 3 details the development and validation of regional FZRA detection algorithms, including the processing of meteorological data to determine threshold values for the algorithms. Section 4 analyses the inter-annual variability of FZRA event activity and demonstrates the application of the algorithms through a case study. Finally, Section 5 offers a summary and conclusions.

2. Materials and Methods

In this study, freezing precipitation, encompassing freezing rain (FZRA) and freezing drizzle (FZDZ), will be referred to as FZRA. FZRA detection algorithms utilize ERA5 reanalysis datasets, applying threshold criteria for air temperature (T) in the melting and sub-freezing layers, relative humidity (RH) at standard isobaric levels in the lower troposphere, surface atmospheric pressure, precipitation rate, and standard deviation of sub-grid scale orography. ERA5 reanalysis datasets, along with standard meteorological measurements, were employed to calibrate and validate the algorithm.

2.1. Weather Station Observations

Data on FZRA events for 20 cold seasons were sourced from standard meteorological observations at 841 weather stations, available in the NOAA archive at <https://www.ncei.noaa.gov/access/search/data-search/global-hourly>, accessed on 21 November 2023. Information on freezing rain and drizzle was extracted from weather reports encoded using the World Meteorological Organization (WMO) international codes: (1) FM-12 SYNOP for weather stations, (2) FM-15 XV METAR for aerodromes [42], and Code KN-01 SYNOP for operational surface meteorological observations from the Federal Service for Hydrometeorology and Environmental Monitoring of the Russian Federation (ROSHYDROMET) weather station network.

FZRA observations were checked at various types of weather stations: manually operated, automatic with partial manual operation, fully automatic, and aviation. Measurements from fully automatic and automatic with partial manual operation weather stations were excluded due to a high probability of errors in precipitation type identification and incomplete observation records (no data from a number of automatic stations for 2004–2024 are available in the NOAA archive). After applying filters (see Section 3.1), 236 weather stations with 4675 FZRA records were selected: 179 manually operated stations (observations at synoptic times with intervals of 3, 6, or 12 h, depending on the station class) and 57 aviation stations (observations at intervals of 1 h or less).

2.2. ERA5 Reanalysis Dataset

The FZRA detection algorithm was developed using the European Centre for Medium-Range Weather Forecasts (ECMWF) ERA5 next-generation reanalysis datasets, which have a spatial resolution of approximately 31 km and an hourly time step. ERA5 is based on the Cy41r2 integrated forecasting system and enhanced observational data assimilation [43]. The following atmospheric parameters were obtained from <https://cds.climate.copernicus.eu/> (accessed on 27 November 2023) and used as predictors: T (°C) and RH (%) at the isobaric levels of 1000, 975, 950, 925, 900, 875, 850, 825, 800, 775, 750, 700, 650, 600, 550, 500 hPa; near surface air temperature at a height of 2 m (T_{2m} , °C); surface atmospheric pressure (P_{surf} , hPa); precipitation rate (P_r , mm/h); standard deviation of sub-grid scale orography (σ_H , m).

3. Algorithm Development

3.1. Processing of Weather Stations Data

The FZRA data were taken from standard observations records at weather stations using WMO codes FM-12 SYNOP and FM-15 METAR. The required data are located in the section of the present weather with the code 7. For manually operated weather stations (codes FM-12 SYNOP), groups were selected with the digital code 24 (freezing rain in the last hour, but not in the time of principal synoptic observation) 56 (light freezing drizzle, glaze ice), 57 (moderate or heavy freezing drizzle, glaze ice), 66 (light freezing rain, glaze ice), and 67 (moderate or heavy freezing rain, glaze ice) at the time of observation. Measurements by automatic weather stations were not included in the dataset (see Section 2.1). Data were selected from the weather reports of aviation weather stations (codes FM-15 METAR) with the letter codes FZRA (freezing rain) and FZDZ (freezing drizzle).

In the national coding version for Russian weather stations, the digital code 79 (glazed rain) was considered. According to the definition of ROSHYDROMET, glazed rain is transparent ice pellets formed because of becoming icing-up droplets in a near-surface air layer with a negative temperature. Upon contact with the surface, the pellets break, and the water flowing out of them freezes and forms an ice crust.

The digital codes 87 and 88 (snow or ice pellets with or without rain or rain and snow in the time of principal synoptic observation) were considered only when recording ice accumulation on the wire of the ice diameter gauge at those meteorological stations where it was available. Data on the glaze ice diameter were selected from the code group 934RR detailed in Section 3, where RR is the diameter in mm. In the absence of data on glaze ice, it is impossible to determine the FZRA presence from the above code digits.

To minimize observational errors, additional filters were applied. Weather stations that recorded an FZRA event only once during the twenty years were filtered out due to the high probability of measurement or coding errors. Individual observations with digits code indicating the presence of FZRA at T_{2m} below $-9\text{ }^{\circ}\text{C}$ or above $4\text{ }^{\circ}\text{C}$ were excluded as erroneous, since for all FZRA events measured, the near surface air temperature was distributed predominantly (97% of cases) in the range from $-9\text{ }^{\circ}\text{C}$ to $4\text{ }^{\circ}\text{C}$, with a median value of $-1\text{ }^{\circ}\text{C}$.

After applying all filters, 4675 FZRA records at 236 weather stations out of 841 were selected. Thus, over the twenty-year observation period, FZRA was recorded by about 28% of weather stations located in the study area.

To estimate the total FZRA amount, the optimal time interval between events was determined by sequentially testing intervals from 3 h to 36 h, with a step of 6 h. The sensitivity of the FZRA amount events to the time intervals is demonstrated in Figure 1. Figure 1a shows the variability in the FZRA total amount events, normalized to their amount at an interval of 3 h, which amounts to 1969 events taken as 100%. The decrease in the FZRA events amount with an increase in the interval from 6 to 24 h is clearly visualized, while an increase in the interval from 24 to 36 h shows practically no effect on its amount.

Hence, this leads to the conclusion that at intervals of 3 h, 6 h, 12 h, and 18 h, there is a possibility of overestimating the FZRA events amount. In addition, weather phenomena occurring in a single synoptic process usually fall within the 24 h interval. Thus, the optimal interval between FZRA events was recognized as $\leq 24\text{ h}$, i.e., FZRA events were defined as one event if the time interval between the last record of the current phenomena and the first record of the subsequent one was no more than 24 h. A similar methodology for identifying the FZRA events number was used by the authors in [30].

The scatter plot of the events amount for the 6-h and 24-h time intervals for each weather station (Figure 1b) shows good agreement between the intervals for weather stations that record no more than 70 FZRA events. Significant discrepancies have three weather stations located in the mountainous regions of China at a height exceeding 1000 m above sea level, where the maximum FZRA amount (more than 100 events) and maximum glazed ice diameter were recorded. The studies [17,18] show that due to the specifics of synoptic processes under the influence of regional topographical features, the duration of FZRA

events increases rapidly at some weather stations in the mountainous regions of China. As a result, FZRA events can continue for more than 24 h. Taking into account the selected time interval of 24 h, the dataset of 1425 FZRA events was formed to calibrate and validate the algorithms.

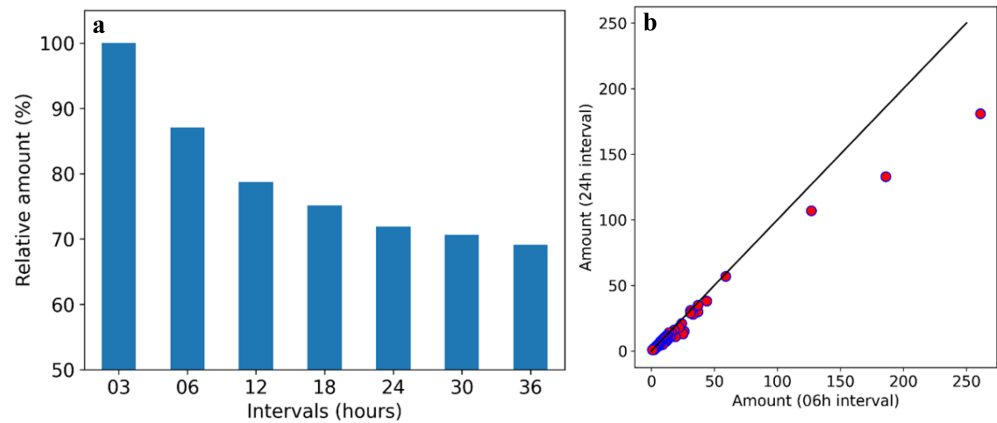


Figure 1. Sensitivity of freezing rain events to time intervals between them: (a) bar plot of the total freezing precipitation amount variability, normalized on the amount at an interval of 3 h (1969 events); (b) the scattering graph of the freezing precipitation events amount at each weather station for the intervals of 6 and 24 h.

Figure 2 shows the spatial distribution and total events amount of FZRA events according to records at weather stations for 20 cold seasons. Weather stations where FZRA events were never recorded or were recorded only once during the twenty-year observation period are visualized as gray circles. Gray circles surrounded by blue lines represent the weather stations that recorded only one FZRA event during the study period. Weather stations that recorded more than one FZRA event during the study period are indicated by colored circles, the size and color of which depend on the events amount according to the color scale. While analyzing the spatial distribution and total amount of FZRA events, it is necessary to keep in mind that the visualized data cannot be considered sufficiently reliable due to disruptions regarding the continuity of meteorological observations at the individual weather stations during the study period. This is the second probable reason for the spatial heterogeneity of FZRA localization, in addition to the influence of feature topography on synoptic processes development (see Section 1).

3.2. Algorithms and Calibration

We utilized the FZRA detection method proposed by Kämäräinen et al. [28], which identifies optimal threshold values for the following environmental parameters: (1) (T_{2m}) —as an indirect indicator of a sub-freezing layer; (2) the T and RH of the above-surface layers to detect a warm layer necessary for melting solid precipitation; (3) Pr ; and (4) the pressure level between the warm and cold layers (P_{cold}). The latter, in conjunction with P_{surf} , allows for the calculation of the cold layer depth ($H_{cold} = P_{surf} - P_{cold}$).

The original method developed by the Finnish Meteorological Institute (hereinafter referred to as the FMIK) is an algorithm designed to estimate FZRA climatology using ERA-Interim reanalysis data across Europe. It analyzes vertical profiles of temperature and humidity from various atmospheric pressure levels (surface, 925, 850, and 700 hPa) to identify the presence of a near-surface cold layer and an above-melting layer. The algorithm utilizes calibrated threshold values, including the minimum cold layer depth (H_{cold}^{thr}), maximum cold layer temperature (T_{i2m}^{thr}), minimum humidity (RH^{thr}), temperature (T_{melt}^{thr}) in the melting layer, and minimum surface precipitation rate (Pr^{thr}). These thresholds were recalibrated based on observations from SYNOP weather stations, where the original subjective values were systematically adjusted through a calibration process to enhance their predictive accuracy.

Here, environmental parameters were obtained from ERA5 reanalysis data for the 236 selected weather stations where at least one FZRA event was recorded over 20 cold seasons. Spatiotemporal matching was conducted using the nearest neighbor method, eliminating duplicate pairs of METAR observations recorded with high frequency ($<30 \text{ min}^{-1}$). The original algorithm calibrated with ERA5 data is referred to as T2MA.

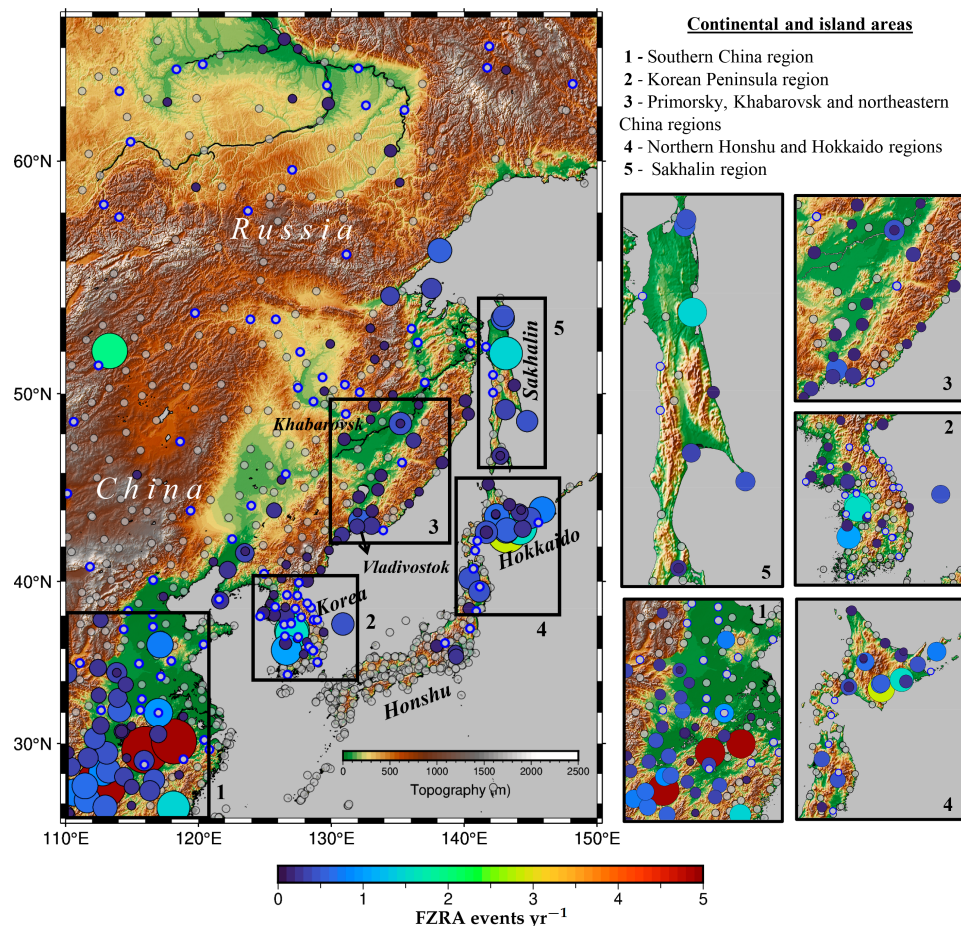


Figure 2. Spatial distribution and total amount of FZRA events for 20 cold seasons (September–May) from 2004 to 2024 by weather stations observations. Black numbered boxes 1 to 5 define areas with weather stations selected for analysis of freezing precipitation events activity.

Due to orography being a significant source of precipitation uncertainty for ERA5 data with a spatial resolution of 31 km [28,44], we excluded areas with high orographic heterogeneity ($\sigma_H > 150 \text{ m}$). This orographic filter reduced the collocated data volume by one-third, yet the correlation coefficient between weather stations and ERA5 T_{t2m} increased significantly to 0.53. Notably, this modest correlation can be observed only in the sample with freezing rain, where the temperature variability is limited (from -9 to $4 \text{ }^\circ\text{C}$).

Another significant factor affecting FZRA detection accuracy is distance to the coastline. Figure 3 demonstrates that during FZRA events in the continental region, the ERA5 T_{2m} values align well with observations, yielding a correlation coefficient of 0.7 and a standard error of 1.3, with median values below zero. In contrast, in the coastal zone, the correlation weakens, and the T_{2m} distribution from the reanalysis shifts toward positive values, indicating a “positive bias”. While approximately 75% of FZRA events recorded by weather stations occurred at negative temperatures, ERA5 data show that only one-third of the events fell within this range.

To enhance the viability of the FMIK method proposed by Kämäräinen et al. [28] as an FZRA detection algorithm for the ERA5 dataset and the selected study area, we developed several modified versions of the method. The proposed modifications included the following:

- The use of ERA5 land skin temperature: Instead of T_{2m} , we calibrated ERA5 land skin temperature (T_{skt}), which exhibits a strong correlation with near-surface air temperature across various spatiotemporal scales [45,46] and is expected to be negative during glaze ice formation in FZRA. Additionally, the T_{skt} in ERA5 shows a less pronounced positive bias in coastal zones compared to observations. This version of the FZRA detection algorithm is denoted as SKTA.
- The inclusion of cold layer temperature: The thresholds of the environmental parameters were supplemented by the minimum temperature in the near-surface cold layer (T_{cold}). This modification is based on the traditional top-down approach commonly used in weather forecasting centers [47]. Here, the calibration of the minimum depth of the near-surface cold layer relies on both T_{cold}^{thr} and T_{melt}^{thr} thresholds. This modified algorithm is referred to as TCLA.
- Majority voting ensemble (MVE) technique: Finally, we applied the MVE technique to combine outputs from T2MA, SKTA, and TCLA, aiming to improve classification and enhance FZRA detection accuracy. In the MVE approach, the resulting prediction is determined by the FZRA label (True/False) that receives the most votes from the individual algorithms, effectively eliminating ties. The MVE approach has been utilized in various fields [48–51]. The MVE technique is referred to as ENSA.

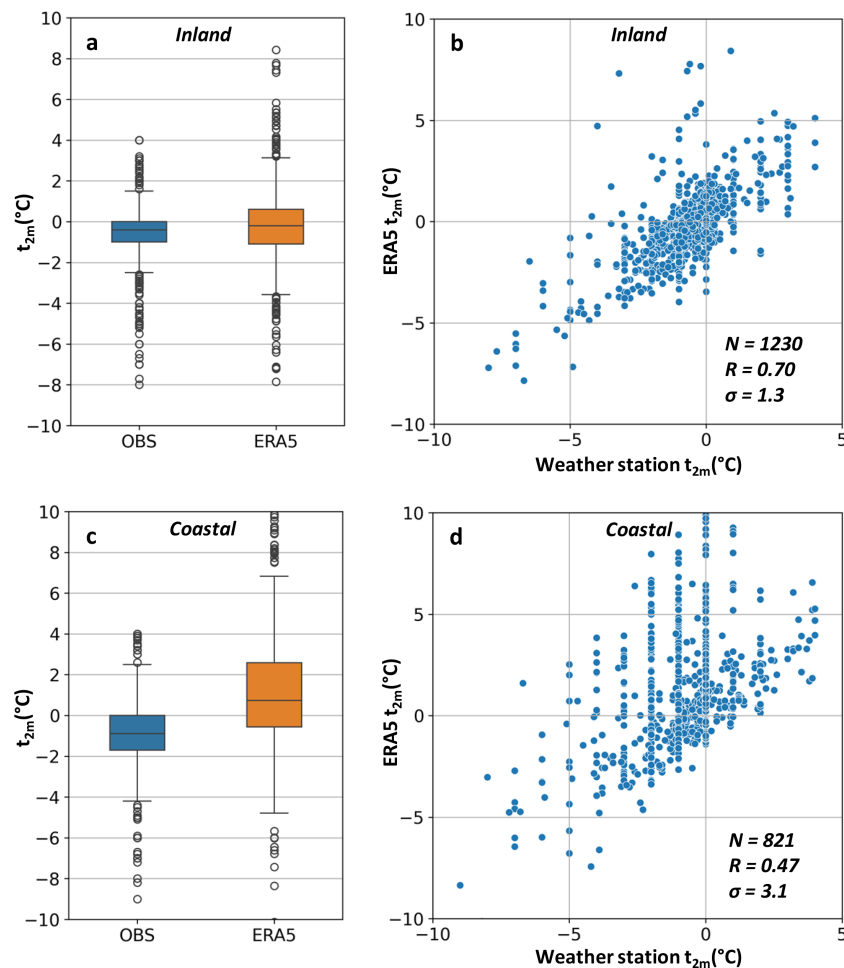


Figure 3. Box (a,c) and scatter (b,d) plots of the collocated near-surface temperature (t_{2m}) obtained from reanalysis dataset (ERA5) and weather station observations (OBSs) in the coastal zone (distance to the coastline is less than 200 km) and inland. Boxes (a,c) indicate the interquartile range, with the horizontal line indicating the median value of t_{2m} . Whiskers extend to the 5th and 95th percentiles, with values outside these ranges plotted as black circles. Some statistics are also given on each scatter plot: number of collocated points (N), correlation coefficient (R) and the root mean square error (σ).

Following the methodology outlined by Kämäräinen et al. [28], we calibrated the threshold values through an iterative looping process, evaluating all combinations of parameter values with sufficient granularity—approximately 1,124,000 distinct threshold combinations. This calibration employed the critical success index (CSI) as a performance metric. The CSI was calculated by comparing the algorithm's outputs with observations of freezing precipitation, which is summarized in a 2×2 contingency table that includes the following: (a) the number of hits, (b) false alarms, (c) misses, and (d) correct rejections (Table 1). The CSI is defined as follows:

$$CSI = \frac{a}{a + b + c} \quad (1)$$

Table 1. Our 2×2 contingency table.

		FZRA Observed	
		True	False
FZRA Detection Algorithm	True	a	b
	False	c	d

Diagnostic algorithms can overestimate the frequency of FZRA events due to the disproportionate weighting of false alarms. This limitation is particularly significant in studies of freezing precipitation climatology, as it may result in the identification of non-existent regions with high FZRA frequency. To address the issue of FZRA overestimation, the absolute value of the bias ($Bias = (a + b)/(a + c)$) is considered on a logarithmic scale [28]. Consequently, the reward function used for calibration (R_{cal}) can be determined by the following formula:

$$R_{cal} = CSI - |\log(Bias)| \quad (2)$$

To develop algorithms for detecting freezing precipitation, we randomly formed two groups of paired reanalysis and observational data from a 20-year period. The first group, consisting of 14 cold seasons, was used to identify the optimal combination of threshold values by maximizing Equation (2). The second group, comprising six cold seasons, was utilized to verify and evaluate the efficiency of the algorithms, including the ENSA method. To improve the statistics and minimize the impact of potential outliers, 12 iterations of calibration and validation were conducted, and these iterations were followed by averaging the threshold values of the relevant parameters and corresponding validation metrics.

Table 2 presents the averaged estimates of the threshold values for the environmental parameters, including T_{melt}^{thr} , RH^{thr} , and P_r^{thr} . These estimates align with typical conditions for FZRA formation [18,52–54] and show good agreement among the proposed algorithms—T2MA, SKTA, and TCLA. During FZRA events, the melting layer contains a relatively warm (≥ 1.3 °C) and humid ($\geq 84\%$) air mass, with possible light precipitation near the surface (starting from 0.01 mm/h). The threshold values for surface temperature (T_{t2m}^{thr} and T_{skt}^{thr}) in the T2MA and SKTA algorithms differ slightly at 0.33° and -0.16° , respectively. The negative value of T_{skt}^{thr} facilitates the freezing of supercooled droplets upon contact with cold surfaces.

Table 2. Comparison of calibrated threshold values of selected environmental variables for three FZRA detection algorithms (T2MA, SKTA, TCLA); the bottom row contains the thresholds obtained by Kämäräinen et al. [28] (FMIK).

Algorithms	T_{melt}^{thr} (°C)	T_{cold}^{thr} (°C)	H_{cold}^{thr} (hPa)	$T_{t2m}^{thr}/T_{skt}^{thr}$ (°C)	P_r^{thr} (mm/h)	RH^{thr} (%)
T2MA	1.4	–	108	0.33	0.02	85
SKTA	1.3	–	112	–0.16	0.01	88
TCLA	1.3	–1.4	27	–	0.02	84
FMIK	–0.64	–	69	0.09	0.065	89

The cold layer depth (H_{cold}^{thr}), which defines the lower boundary of the melting layer, requires special attention. In the T2MA and SKTA algorithms, the calibrated H_{cold}^{thr} value is unrealistically large at 112 hPa (over 1000 m), which is a value more typical for ice pellet formation [55]. A similar issue was noted in [28], albeit with a smaller discrepancy (69 hPa). We propose that the original algorithm calibrates H_{cold}^{thr} based on the warm layer’s characteristic temperature, neglecting the impact of the cold layer and resulting in a significant overestimation. In contrast, the TCLA algorithm, which considers the subfreezing layer temperature, yielded a much smaller minimum H_{cold}^{thr} of 27 hPa (approximately 220 m). Roberts and Stewart [55] demonstrated that the cold layer depth during freezing precipitation events can vary widely from 180 to 1500 m, with a median of about 850 m. Slightly smaller estimates (around 700 m) were reported in [52]. It is important to note that the ERA5’s vertical resolution in the lower troposphere is 25 hPa [43], which complicates the accurate representation of thinner layers.

3.3. Detection Skill Evaluation

To directly compare the different algorithms, we computed key quality measures, as described in [56]. In addition to the critical success index (CSI) and bias (defined above), we included the Probability of Detection (POD) and Success Ratio (SR), which are defined as follows:

$$POD = \frac{a}{a + c} , \tag{3}$$

$$SR = 1 - \frac{b}{a + b} . \tag{4}$$

We also incorporated the Heidke Skill Score (HSS) as an additional evaluation metric [57], which is useful for comparing precipitation-type forecasts [58–60].

Table 3 compares the performance of the five FZRA detection algorithms and the ERA5 precipitation-type product across selected validation periods. The results show significant variation in detection skill, as indicated by the CSI, with values ranging from 0.084 to 0.133; the ERA5 product exhibited the lowest skill. Notably, the TCLA and ENSA methods achieved the highest CSI and HSS values of 0.133 and 0.234, respectively. But the MVE-based ENSA technique also demonstrated the fewest false alarms—reflected in an SR of 0.266. These results highlight the advantage of the ENSA in its reliability of FZRA events detection.

Table 3. Comparison of verification statistics for six FZRA detection algorithms and corresponding weather station observations in validation periods. Key quality measures of the algorithm include the critical success index (CSI), the probability of detection (POD), success ratio (SR or $1 - \text{false alarm ratio}$) and bias, as described in [56]; the table also includes the Heidke Skill Score (HSS) as the additional evaluation metric [57].

Quality Measures	T2MA	SKTA	TCLA	ENSA	FMIK	ERA5
CSI	0.132 ± 0.032	0.117 ± 0.023	0.133 ± 0.029	0.133 ± 0.030	0.104 ± 0.024	0.084 ± 0.020
POD (%)	22 ± 5	21 ± 4	22 ± 4	22 ± 5	25 ± 6	23 ± 4
SR	0.247 ± 0.054	0.209 ± 0.042	0.256 ± 0.052	0.262 ± 0.055	0.152 ± 0.036	0.116 ± 0.031
Bias	0.90 ± 0.15	1.02 ± 0.17	0.85 ± 0.12	0.82 ± 0.14	1.66 ± 0.36	2.11 ± 0.46
HSS	0.232 ± 0.050	0.208 ± 0.037	0.234 ± 0.045	0.234 ± 0.047	0.186 ± 0.040	0.154 ± 0.035

To further substantiate our claims, we performed a paired *t*-test for the CSI and HSS values of the ENSA and TCLA algorithms compared to the original FMIK method and ERA5 product. The results provide robust statistical evidence supporting our assertion that both the ENSA and TCLA algorithms outperform traditional methods in detecting freezing precipitation (*p*-value < 0.05).

Both the original FMIK algorithm and the ERA5 product demonstrated superior skill only in terms of their probability of detection (POD) results. However, they overestimated FZRA amounts by factors of 1.8 to 2.1 (see Table 3 regarding the bias metric), which limits their applicability in climate studies. In contrast, the SKTA algorithm showed a lower bias (bias = 1.01) while maintaining a POD value comparable to the other modified algorithms. This advantage may allow the SKTA algorithm to more accurately reproduce average FZRA frequency estimates over large regions, enhancing its utility in climatological assessments.

4. Application of the Freezing Precipitation Detection Algorithm

4.1. Freezing Precipitation Events Activity

To analyze the inter-annual variability of the spatially averaged freezing precipitation activity over a twenty-year period, five areas characterized by high activity levels and closely situated weather stations were selected (Figure 2). Based on their geographical location, these areas were categorized into three continental regions (Areas 1–3) and two island regions (Areas 4 and 5). The proximity of weather stations within these areas enhances the likelihood of capturing the current synoptic process.

Area 1 includes weather stations in the south of China. During the calibration and validation stages of the algorithms, three stations located at elevations exceeding 1000 m above sea level, which recorded the highest amounts and durations of FZRA events, were excluded due to significant topographic heterogeneity (see Section 3.2). Area 2 consists of weather stations on the Korean Peninsula and Ulleungdo Island. Area 3 encompasses stations in the Primorsky and Khabarovsk regions. Island weather stations are grouped into Area 4, which includes Northern Honshu, Hokkaido, and the Southern Kuril Islands, and Area 5 covers the Sakhalin Island.

The ability of the algorithms to reproduce the inter-annual variability of the spatially averaged FZRA amount was evaluated using weather station observations across the five designated areas. Additionally, the four algorithms developed in this study were compared with the FMIK algorithm—the original method developed at the Finnish Meteorological Institute—as well as with the ERA5 precipitation-type product.

In continental Areas 1 and 3, all algorithms and the ERA5 product demonstrated a stable correlation with the weather station observations (Table 4). The SKTA algorithm achieved the best results, with correlation coefficients of $R = 0.96$ for Area 1 and $R = 0.89$ for Area 3, and minimal root mean square error (σ) of 0.58 and 0.25, respectively. The high correlation in Area 1 ($R > 0.90$ for all algorithms) is likely due to the large number of weather stations and the ability of ERA5 to reproduce the conditions for FZRA occurrence.

Table 4. Evaluation of the algorithms’ ability to reproduce inter-annual variability of spatially averaged freezing precipitation in the allocated areas (see Figure 2) compared to weather stations observations. The coefficient of correlation (R), coefficient of determination (R^2), and the root mean square error (σ) were calculated for each area and for all areas together. The best statistics for the corresponding algorithm are highlighted in bold.

	Area 1		Area 2		Area 3		Area 4		Area 5		All Areas		
	R	σ	R	R^2	σ								
T2MA	0.95	0.70	0.64	0.18	0.86	0.29	0.49	0.63	0.38	0.53	0.93	0.72	0.24
SKTA	0.96	0.58	0.30	0.19	0.89	0.25	0.51	0.47	0.41	0.41	0.95	0.80	0.20
TCLA	0.95	0.73	0.37	0.21	0.85	0.28	0.51	0.68	0.27	0.62	0.92	0.72	0.24
ENSA	0.95	0.63	0.44	0.20	0.86	0.27	0.47	0.65	0.37	0.56	0.93	0.70	0.25
FMIK	0.90	1.14	0.70	0.15	0.81	0.71	0.43	0.55	0.28	0.47	0.86	0.23	0.40
ERA5	0.92	1.28	0.28	0.61	0.74	0.61	0.36	0.47	0.27	0.41	0.89	−0.30	0.52

In Area 2, only two algorithms showed stable correlations, one of which (FMIK) is not regionally adapted. The FMIK algorithm achieved the highest correlation ($R = 0.70$), while among the regional algorithms, T2MA was the most effective with $R = 0.64$. The relatively poor performance of some algorithms may be attributed to the geographical location of the Korean Peninsula, which extends far into the sea. Consequently, most weather stations in Area 2 are located in coastal zones, where reanalysis indicates a shift in near-surface air temperatures toward positive values (Figure 3c).

In island Areas 4 and 5, all algorithms exhibited weakly stable or unstable correlations with large root mean square errors (Table 4). In Area 4, the SKTA and TCLA algorithms performed best ($R = 0.51$), with SKTA having the lowest error ($\sigma = 0.47$). In Area 5, SKTA achieved the maximum correlation ($R = 0.41$) with a minimum σ of 0.41.

Overall, in continental areas, the algorithms effectively reproduce the inter-annual variability of spatially averaged FZRA activity. However, there was a significant decrease in performance in the island areas. Although the Korean Peninsula is formally classified as a continental area, its geographical position between continental and island regions affected the efficiency of the algorithm. While nearly half of the algorithms yielded stable correlations, the R values are lower than those in continental areas but higher than those in island areas.

Among the regional algorithms, TCLA and ENSA were the most effective in detecting FZRA events, while SKTA excelled in reproducing their spatially averaged inter-annual variability, as evidenced by its optimal bias value of 1.01 (Table 3). The FMIK algorithm and the ERA5 product demonstrated the best results in terms of the POD value (Table 3), but they significantly overestimated the detected FZRA events due to the large number of false alarms.

On average, across all areas, the algorithms exhibited a stable correlation, with R values comparable to those observed in Area 1. This is likely due to the substantial contribution of Area 1 to the total FZRA amount, which can be attributed to its dense network of weather stations. However, the regional algorithms demonstrated even higher correlations. The coefficients of determination indicate that only the T2MA, SKTA, TCLA, and ENSA algorithms exhibited a significant relationship between model outputs and meteorological observations, with R^2 values ranging from 0.70 to 0.80.

The SKTA algorithm consistently provided the best results in reproducing the inter-annual variability of FZRA events across almost all areas. In contrast, the FMIK algorithm and the ERA5 precipitation-type product showed much lower R^2 values, with the ERA5 product even exhibiting negative R^2 values. The latter indicates that the predictions made by the product perform worse than a simple mean-based prediction. In the context of this study, this suggests that the ERA5 product failed to capture the inter-annual variability of FZRA events over the Far East, possibly due to inherent biases (Table 3) and limitations in its precipitation-type classification.

A comparative analysis of the inter-annual variability of FZRA events across the designated areas, based on meteorological observations and the SKTA algorithm, demonstrates high effectiveness of the algorithm both for the entire area ($R = 0.95$, $\sigma = 0.2$, as shown in Figure 4a) and specifically in Area 1 ($R = 0.96$, $\sigma = 0.58$, as shown in Figure 4b). The analysis indicates that the algorithm consistently overestimated FZRA activity during peak periods and underestimated it during low periods. In other areas, the model predominantly underestimated FZRA activity, with exceptions in certain seasons.

In Area 2 (Figure 4c), given the weak correlation ($R = 0.3$), the algorithm significantly underestimated FZRA activity in four cold seasons and did not detect it in eight ones. In Area 3 (Figure 4d), the algorithm significantly overestimated FZRA activity during the 2020–2021 season and underestimated it during the 2023–2024 season. In the island regions, Areas 4 (Figure 4e) and 5 (Figure 4f), there was a noticeable underestimation of FZRA activity by the algorithm. It is noteworthy that in Area 4, FZRA was not detected only in one season (2023–2024).

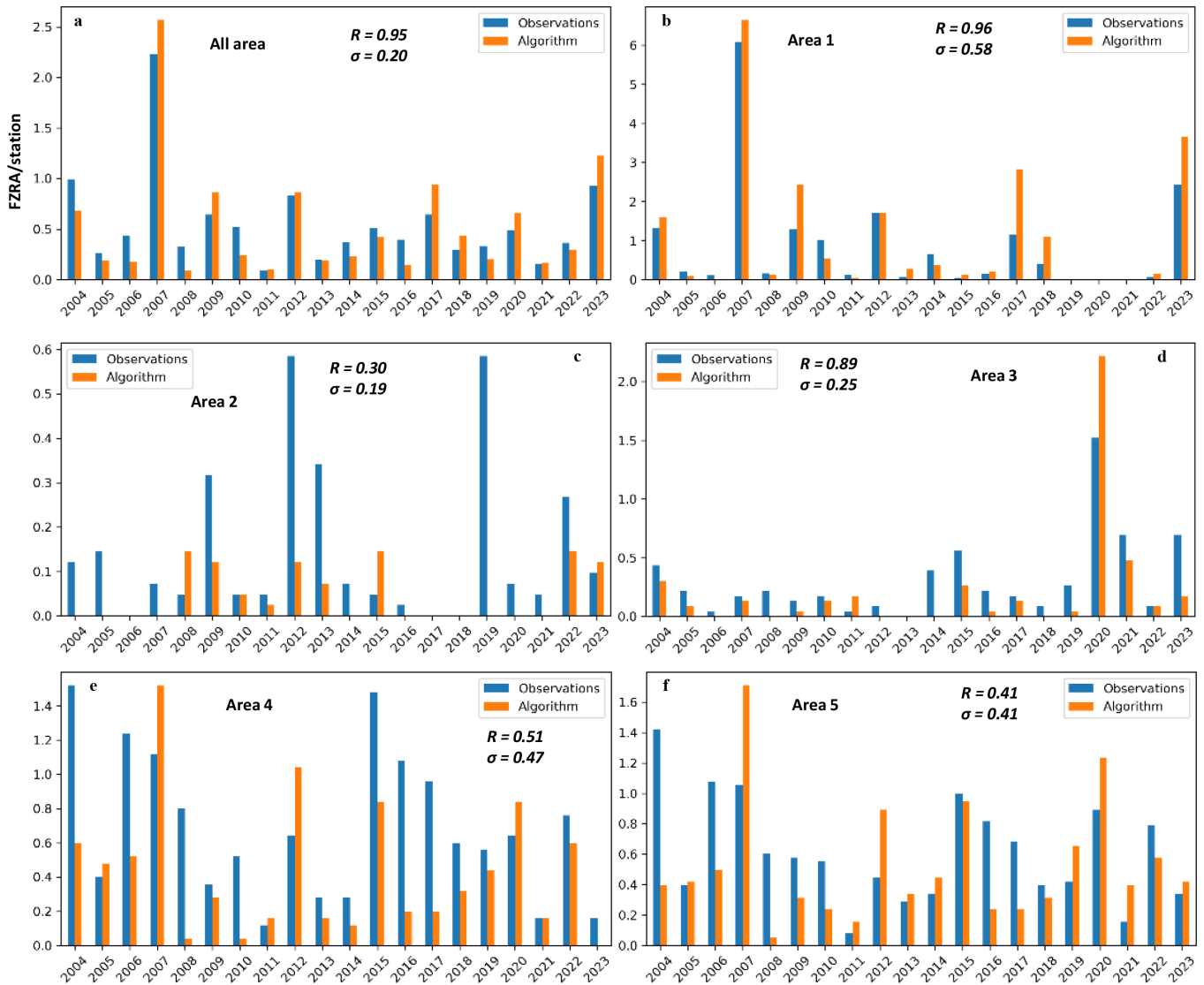


Figure 4. Inter-annual variability of FZRA activity over 20 years based on weather station observations (blue) and the algorithm (orange): (a) total FZRA events amount in five areas. (b) Area 1 (China). (c) Area 2 (Korean Peninsula and Ulleungdo Isl.). (d) Area 3 (Primorsky and Khabarovsk regions). (e) Area 4 (Northern Honshu, Hokkaido, and Southern Kuril Isl.). (f) Area 5 (Sakhalin). R —correlation coefficient. σ —the root mean square error. The y axis is area-averaged mean FZRA amount per station.

4.2. Case Study

The effectiveness of the FZRA detection algorithms is shown by the case study of a typical “southern” synoptic process in November. The November “southern” cyclones coming out of northeastern China to the Primorsky and Khabarovsk regions usually create conditions for FZRA events. The selected FZRA case is provided with nearly simultaneous meteorological observations, upper-air sounding data, and satellite measurements, contributing to a detailed examination. Moreover, the features of the FZRA evolution allowed us to reveal both the strengths and weaknesses of the reanalysis-based diagnostic method.

An FZRA and ice glaze event, recorded at 12 weather stations in China and Russia on 7–9 November 2021, led to damage to power lines supports and broken wires. As a result, 21 settlements on Russian territory were left without electricity. This event was caused by an active cyclone that occurred over China. As recorded in upper-air maps, the cyclone developed under the front part of a deep upper-level trough, in the southern part of which a deep upper-level depression formed. The expressed meridionality of the synoptic process contributed to strong thermal asymmetry and, as a consequence, the advection of warm

and humid air masses in front of the cyclone, as well as intense cold advection that occurred in its rear.

As the cyclone moved northeast, freezing precipitation was observed on 7–8 November at three weather stations in China and on 8–9 November at nine weather stations in Russia. The FZRA information from 3 of the 12 weather stations is missing in the NOAA archive. In general, four of the algorithms detected FZRA at seven of the nine weather stations, which make up a total of 78% their overall efficiency. Of these, T2MA and TCLA detected FZRA at five weather stations and ENSA at six ones, and the most effective was SKTA, which detected FZRA at seven weather stations.

According to observations, 37 records of FZRA were made at seven weather stations. As for the algorithms, T2MA and ENSA yielded 21 hits, as well as 12 and 11 false hits, respectively. The best result was SKTA—which yielded 22 hits—the worst result was shown by TCLA at 18 hits, and both algorithms yielded nine false hits. For comparison, the ERA5 product yielded only 18 hits and 62 false hits. This is consistent with the tendency of reanalysis to produce significantly more false FZRA detections than the algorithms mentioned in Section 3.3.

Figure 5 demonstrates the cyclone location on the surface analysis map at 00 UTC (Figure 5a) and its cloud system on the infrared image obtained by the AVHRR radiometer onboard the MetOp-B satellite at 01:25 UTC (Figure 5b) on 8 November. On 7–8 November, the weather stations in the Changchun and Harbin airports recorded FZRA continuously for 9 h and 6 h, respectively. The weather station at the Khabarovsk airport recorded FZRA and FZDZ events during the period of 20:30–13:30 UTC on 8–9 November with interruption, taking into account when freezing precipitation lasted for about 5 h.

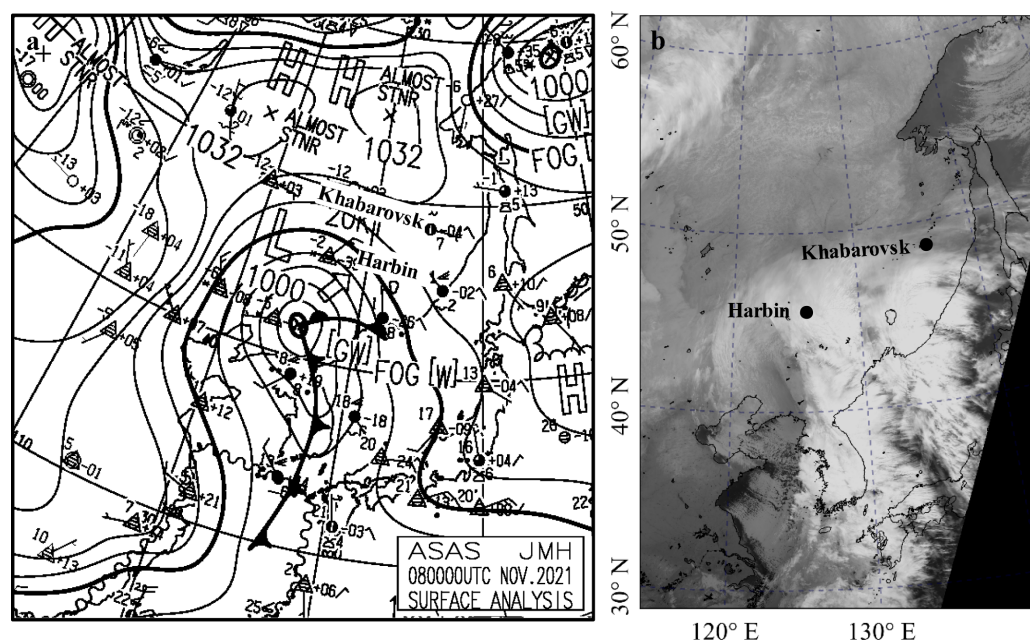


Figure 5. Surface analysis map of JMH (Japan Meteorological and Hydrographic Agency) at 00 UTC (a); the cloud system of cyclone on the infrared image (band 4, 10.82 μm) obtained by AVHRR onboard satellite MetOp-B at 01:25 UTC (b) on 8 November 2021.

The temporal variability graphs of meteorological elements for the periods on 5–10 November at the weather station records in the Harbin airport (Figure 6a) and on 6–11 November at the weather station records at the Khabarovsk airport (Figure 6b) show a rapid decrease in the near surface air temperature one day before the FZRA onset in Harbin and two days before its onset in Khabarovsk. In Harbin, the T_{2m} decreased by 19 °C (from 13 °C at 06 UTC on 5 November to −6 °C at 21 UTC on 6 November); in Khabarovsk, it decreased by 18 °C (from 9 °C at 03 UTC to −9 °C at 18 UTC on 6 November). Then, during the day before the FZRA started, an insignificant increase in the T_{2m} was observed

to values not higher than 0 °C. During the fallout, the T_{2m} varied in the range from −2 °C to −1 °C in Harbin and from −1 °C to 0 °C in Khabarovsk.

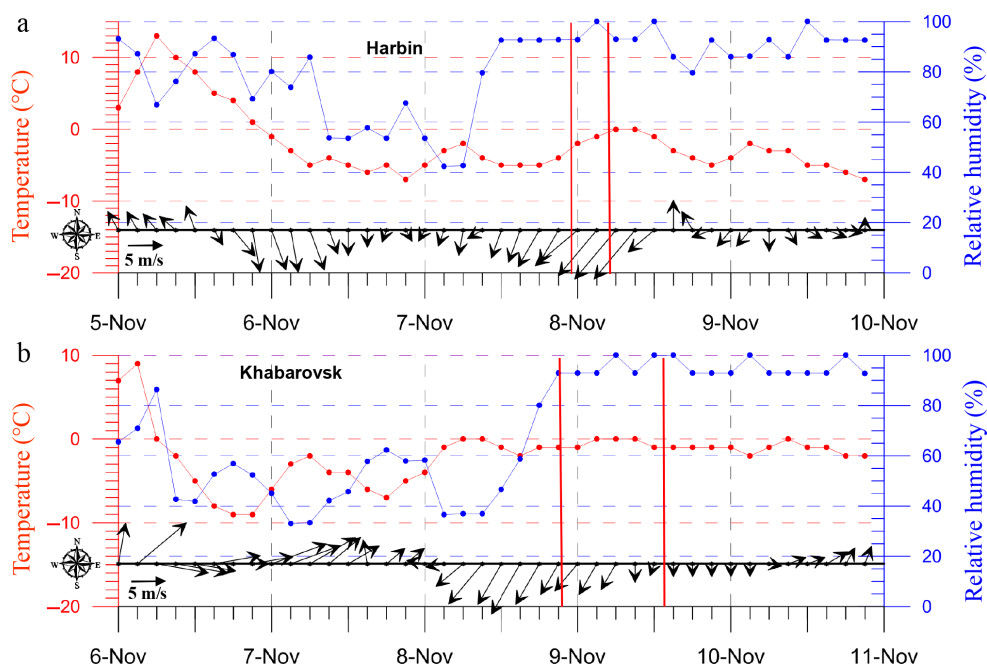


Figure 6. The temporal variability of meteorological elements (surface air temperature [red lines], relative humidity [blue lines], wind speed and direction [black arrows]) approximately three days before the onset of the FZRA, during precipitation, and approximately two days after its end in Harbin (a) and Khabarovsk (b). The red vertical lines indicate the period of the freezing precipitation.

In Harbin, freezing precipitation detected by TCLA lasted from 23 UTC on 7 November to 05 UTC on 8 November. According to radiosonde (RS) data recorded at 00 UTC on 8 November, there was an advective temperature inversion. The melting layer thickness was about 570 m, with a maximum temperature of $T_{max} = 1.3$ °C at an altitude of 1045 m, and the freezing layer thickness was about 800 m, with a minimum temperature of $T_{min} = -5.9$ °C at an altitude of 684–732 m. According to the RS data recorded at 12 UTC on 8 November, the melting layer lacked.

In Khabarovsk, freezing precipitation was detected by T2MA and continued intermittently from 20:30 UTC on 8 November to 13:30 UTC on 9 November. According to the RS data (not presented), at 12 UTC on 8 November, there was an advective temperature inversion. The melting layer thickness was registered at about 700 m, with $T_{max} = 2.6$ °C at an altitude of 934 m. The freezing layer thickness was registered at about 450 m, with $T_{min} = -2.7$ °C at an altitude of 337 m.

At 00 UTC on 9 November, the melting layer thickness increased by more than 1400 m, and the T_{max} increased to 5.6 °C at an altitude of 818 m. In this case, the freezing layer thickness decreased to about 190 m, and the T_{min} dropped to −2.1 °C and was recorded at an altitude of 258 m. At 12 UTC on 9 November, the melting layer thickness began to decrease and was registered at about 680 m, with $T_{max} = 4.2$ °C at an altitude of 667 m, and the freezing layer thickness was registered at 170 m, with $T_{min} = -2.1$ °C at an altitude of 242 m. At 00 UTC on 10 November, the normal gradient with negative temperature values came back.

Less than a day before the FZRA started, a rapid increase in relative air humidity to 90–100% was recorded at both stations (Figure 6). After freezing precipitation ceased, the T_{2m} did not rise above 0 °C, the RH exceeded 80%, and freezing fog was recorded in Khabarovsk. The wind changed direction from southeast to north 56 h before the FZRA onset in Harbin and from southwest to northeast 21 h before in Khabarovsk, which would

be associated with a slowdown in the cyclone's movement speed. Freezing precipitation fell with weak and moderate northeastern winds.

Based on the RS and ERA5 data, vertical profiles of air temperature T (stratification curve: red) and dew points T_d (green) were obtained for Harbin and Khabarovsk (Figure 7). The solid line denotes the T and T_d registered from the ERA5 data, and the dotted line denotes the RS data. The T and T_d vertical profiles show favorable conditions for FZRA. According to the ERA5 data at 00 UTC on 8 November, in Harbin, the freezing layer with a thickness of 100 hPa was clearly defined in the negative temperatures area (Figure 7a). The air temperature in the melting layer with a thickness of about 70 hPa was in the range of 0–1 °C. The distribution of the T , T_d , and the thicknesses of the freezing and melting layers are in good agreement with the RS data for the same period.

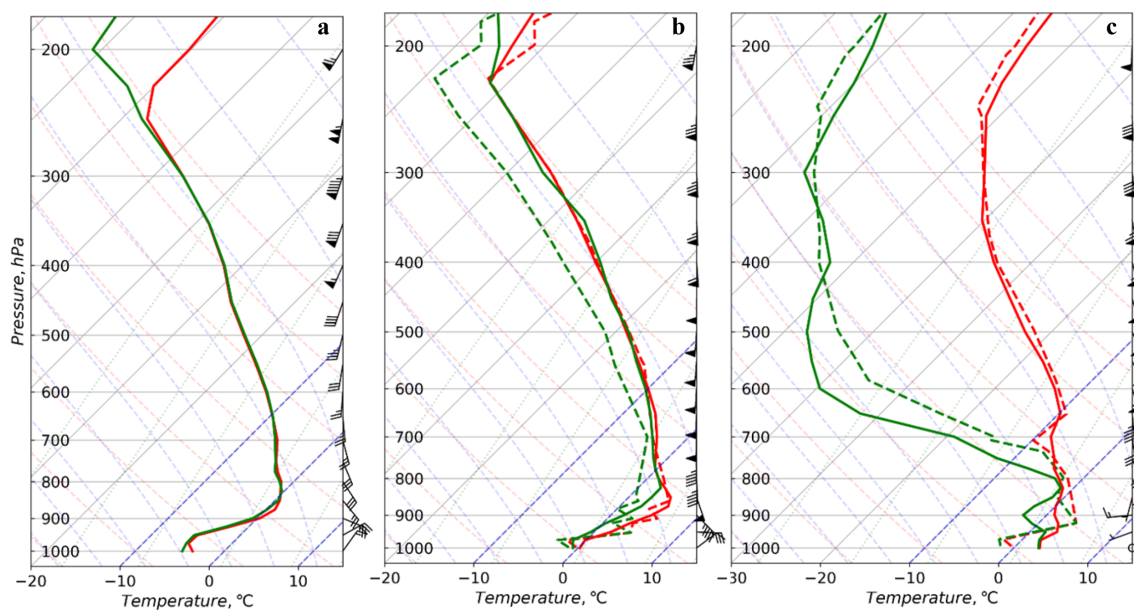


Figure 7. Vertical profiles on skew-T diagram of air temperature (red) and dew point temperature (green) from ERA5 (solid lines) and upper-air sounding (dashed lines) at 00 UTC on 8 November 2021 in Harbin (a); at 23 UTC on 8 November 2021 (b); and at 12 UTC on 9 November 2021 in Khabarovsk (c).

A comparative analysis of the T and T_d vertical profiles from the ERA5 data at 23 UTC on 8 November and RS data at 00 UTC on 9 November in Khabarovsk demonstrates a coincidence of the freezing layers thickness values of 30 hPa (Figure 7b). The air temperature in the freezing layer derived from the ERA5 data is 1 °C higher than that of the RS data, but it did not exceed 0 °C. It corresponds to the threshold values of the algorithm. The stratification curves derived from the ERA5 and RS data practically coincide in the melting layer and further up to the tropopause.

At 12:00 UTC on 9 November, freezing rain began to weaken and transformed into freezing drizzle (FZDZ). The RS vertical temperature profile shows that the freezing and melting layers were clearly defined, while according to the ERA5 data, the air temperature was shifted to the positive values area (Figure 7c). Thus, despite the favorable conditions for freezing precipitation and their presence according to meteorological observations, they were not detected either by the algorithms or by reanalysis.

5. Discussion and Conclusions

This study introduced four regional algorithms for detecting FZRA in the Far East region, encompassing part of China, the Korean Peninsula, the Ulleungdo Island, Japan, and part of the Russian Far East region. These algorithms were developed using the ERA5 dataset and standard meteorological measurements over 20 cold seasons (September–May)

from 2004 to 2024. Previous studies on freezing precipitation in the Far East have been limited in scope, lacking comprehensive climate research. These regional algorithms are intended for use in climate and statistical studies of freezing precipitation in this area.

We utilized the FZRA detection method proposed by Kämäräinen et al. [28] and calibrated optimal threshold values for the ERA5 environmental parameters, such as the near-surface air temperature, vertical profiles of temperature and relative humidity, surface precipitation rate, and surface pressure, to effectively identify the conditions favorable for FZRA occurrence.

To improve the diagnostic algorithm's applicability to the ERA5 dataset, we implemented modifications, including replacing the near-surface temperature metric with the ERA5 land skin temperature metric, as well as incorporating the minimum temperature metric from the near-surface cold layer, following a traditional top-down approach commonly used in weather forecast centers [47]. Additionally, a majority voting ensemble (MVE) technique was applied to integrate outputs from multiple algorithms, enhancing classification accuracy.

Validation of the modified algorithms (T2MA, TCLA, SKTA, and ENSA) showed significant improvements over the original method FMIK developed at the Finnish Meteorological Institute. The ENSA algorithm, based on the majority voting ensemble technique, achieved the best verification statistics, with percentage increases in the CSI (HSS) quality measure of 66% (51%) and 21% (18%) compared to the ERA5 precipitation-type product and the FMIK algorithm, respectively. Furthermore, the SKTA algorithm demonstrated a notable advantage in reproducing average estimates of FZRA frequency across large regions, thereby enhancing its utility in climatological assessments. It is important to note that the calibrated threshold values, while physically justified, were adjusted based on ERA5 data and are thus sensitive to potential model biases. This sensitivity partly explains the significant discrepancies with the threshold values reported by Kämäräinen et al. [28].

The regional algorithms developed in this study effectively reproduced the inter-annual variability of spatially averaged FZRA activity in continental areas, with correlation coefficients ranging from 0.95 to 0.96. However, their effectiveness decreased significantly in island regions, where their correlation coefficients range from 0.27 to 0.51. The Korean Peninsula, due to its geographical location, serves as a transition zone between continental and island conditions, impacting algorithm performance with correlation coefficients between 0.44 and 0.64. This reduced effectiveness is attributed to the concentration of weather stations in coastal areas, where ERA5 data show a marked shift in surface air temperature towards positive values (Figure 3c). Notably, the FMIK algorithm exhibited the highest correlation on the Korean Peninsula and Ulleungdo Island ($R = 0.70$), while among regional algorithms, T2MA was the most effective ($R = 0.64$).

The coefficients of determination (R^2) indicate significant predictive validity for the regional algorithms, varying between 0.70 and 0.80. In contrast, low R^2 values for the FMIK algorithm and negative values for the ERA5 product suggest weak or absent predictive validity. While the TCLA and ENSA were most effective in detecting FZRA, the SKTA excelled in reproducing spatially averaged inter-annual variability, as evidenced by its optimal bias value (bias = 1.01) compared to the other regional algorithms (Table 3). A comparative analysis of inter-annual variability, based on the meteorological observations and SKTA, demonstrated high algorithm effectiveness across all areas, with an overestimation at FZRA activity peaks and an underestimation at the minima. In other regions, the SKTA underestimated the FZRA activity in approximately 50% of the seasons.

The effectiveness of regional algorithms was further demonstrated in a case study examining the dates of 7–9 November 2021 at weather stations in China and Russia. Out of 37 FZRA records, the T2MA and ENSA yielded 21 hits, with 12 and 11 false hits recorded, respectively. The SKTA yielded 22 hits, and the TCLA yielded 18 hits, and each one yielded nine false hits. The ERA5 product yielded 18 hits but also 62 false hits, highlighting its tendency to overpredict FZRA events compared to the algorithms.

The key quality indicators of the regional freezing precipitation detection algorithms suggest their potential use in both operational activities and climatological assessments. With comparable scores for the CSI, POD, and SR metrics (Table 3), the TCLA and ENSA yielded slightly better results in FZRA detection. For climatological and statistical assessments, the SKTA is preferable due to its superior performance in average estimates. In addition, the developed regional algorithms can be used to assess the inter-annual and long-term variability of freezing precipitation event activity in the Far East region.

Author Contributions: Conceptualization and design experiments, M.P. and I.G.; processing and visualization of satellite data and weather stations observations, A.B., V.K. and E.K.; I.G. and M.P. analyzed the data and wrote the paper; M.P. visualized results and edited and reviewed the paper. All authors have read and agreed to the published version of the manuscript.

Funding: This work was supported by the Russian state budget theme 124022100080-0 and the program 123072000039-5 “Development of a climate monitoring system for the Russian Far Eastern seas and the northwestern Pacific Ocean based on multi-platform observations and operational hydrodynamic modeling”.

Data Availability Statement: Standard meteorological observations at weather stations, available in the NOAA archive at <https://www.ncei.noaa.gov/access/search/data-search/global-hourly> (accessed on 21 November 2023) and ERA5 hourly fields, can be found at <https://cds.climate.copernicus.eu/> (accessed on 27 November 2023), respectively.

Acknowledgments: This research was supported in part through computational resources provided by the Pacific Oceanological Institute in Vladivostok.

Conflicts of Interest: The authors declare no conflicts of interest.

References

1. Simonson, J. *Extratropical Cyclones and Associated Climate Impacts in the Northeastern United States*; The University of Maine: Orono, ME, USA, 2020.
2. Huffman, G.J.; Norman, G.A., Jr. The supercooled warm rain process and the specification of freezing precipitation. *Mon. Weather Rev.* **1988**, *116*, 2172–2182. [[CrossRef](#)]
3. Rauber, R.M.; Olthoff, L.S.; Ramamurthy, M.K.; Kunkel, K.E. The relative importance of warm rain and melting processes in freezing precipitation events. *J. Appl. Meteorol. Climatol.* **2000**, *39*, 1185–1195. [[CrossRef](#)]
4. Matsushita, H.; Nishio, F. A simple method of discriminating between occurrences of freezing rain and ice pellets in the Kanto Plain, Japan. *J. Meteorol. Soc. Jpn. Ser. II* **2008**, *86*, 633–648. [[CrossRef](#)]
5. Lu, Z.; Han, Y.; Liu, Y. Occurrence of warm freezing rain: Observation and modeling study. *J. Geophys. Res. Atmos.* **2022**, *127*, e2021JD036242. [[CrossRef](#)]
6. Klima, K.; Morgan, M.G. Ice storm frequencies in a warmer climate. *Clim. Chang.* **2015**, *133*, 209–222. [[CrossRef](#)]
7. Adhikari, A.; Liu, C. Remote sensing properties of freezing rain events from space. *J. Geophys. Res. Atmos.* **2019**, *124*, 10385–10400. [[CrossRef](#)]
8. Bragg, D.C.; Shelton, M.G.; Zeide, B. Impacts and management implications of ice storms on forests in the southern United States. *For. Ecol. Manag.* **2003**, *186*, 99–123. [[CrossRef](#)]
9. Klopčič, M.; Poljanec, A.; Dolinar, M.; Kastelec, D.; Bončina, A. Ice-storm damage to trees in mixed Central European forests: Damage patterns, predictors and susceptibility of tree species. *For. Int. J. For. Res.* **2020**, *93*, 430–443. [[CrossRef](#)]
10. Ivanov, A.; Zamolodchikov, D.; Kravchenko, O.; Soloviev, I. Impact of Ice Rain on Forests of Russky Island. *Russ. J. Ecol.* **2024**, *55*, 71–78. [[CrossRef](#)]
11. DeGaetano, A.T. Climatic perspective and impacts of the 1998 northern New York and New England ice storm. *Bull. Am. Meteorol. Soc.* **2000**, *81*, 237–254. [[CrossRef](#)]
12. Cortinas, J. A climatology of freezing rain in the Great Lakes region of North America. *Mon. Weather Rev.* **2000**, *128*, 3574–3588. [[CrossRef](#)]
13. Kämäräinen, M.; Hyvärinen, O.; Vajda, A.; Nikulin, G.; Meijgaard, E.v.; Teichmann, C.; Jacob, D.; Gregow, H.; Jylhä, K. Estimates of present-day and future climatologies of freezing rain in Europe based on CORDEX regional climate models. *J. Geophys. Res. Atmos.* **2018**, *123*, 13–291. [[CrossRef](#)]
14. Leonov, I.; Sokolikhina, N. Ice storm formation conditions in Vladivostok in November 2020, *Gidrometeorol. Issled. Prognozy* **2021**, *4*, 69–83.
15. Gurvich, I.; Pichugin, M.; Baranyuk, A.; Khazanova, E. Ice storm in Primorye on November 18–19, 2020. *Curr. Probl. Remote Sens. Earth Space* **2021**, *18*, 241–252. [[CrossRef](#)]

16. Deng, D.; Gao, S.; Du, X.; Wu, W. A diagnostic study of freezing rain over Guizhou, China, in January 2011. *Q. J. R. Meteorol. Soc.* **2012**, *138*, 1233–1244. [[CrossRef](#)]
17. Deng, D.; Gao, S.; Hu, L.; Du, X.; Wang, J.; Wang, C. The impact of Guizhou topography on the distribution of freezing rain in early January 2011. *Q. J. R. Meteorol. Soc.* **2015**, *141*, 3252–3267. [[CrossRef](#)]
18. Zhou, Y.; Yue, Y.; Gao, Z.; Zhou, Y. Climatic characteristics and determination method for freezing rain in China. *Adv. Meteorol.* **2017**, *2017*, 4635280. [[CrossRef](#)]
19. Kwon, H.N.; Byun, H.R.; Park, C.K. Case studies on freezing rain over the Korean Peninsula using KLAPS. *Atmosphere* **2015**, *25*, 389–405. [[CrossRef](#)]
20. Park, C.K.; Byun, H.R. Three cases with the multiple occurrences of freezing rain in one day in Korea (12 January 2006; 11 January 2008; and 22 February 2009). *Atmosphere* **2015**, *25*, 31–49. [[CrossRef](#)]
21. Matsushita, H.; Nishio, F. Climatological characteristics and local influences on occurrence of freezing precipitation in Japan. *J. Jpn. Soc. Snow Ice* **2004**, *66*, 541–552. [[CrossRef](#)]
22. Wen, Q.H.; Wan, D.; Dong, Q.; Yan, Y.; Zhang, P. Improved freezing rain forecast using machine learning. *Weather Clim. Extrem.* **2024**, *44*, 100690. [[CrossRef](#)]
23. Kwon, S.H.; Byun, H.R.; Park, C.K.; Kwon, H.N. On the freezing precipitation in Korea and the basic schemes for its potential prediction. *Asia-Pac. J. Atmos. Sci.* **2016**, *52*, 35–50. [[CrossRef](#)]
24. Robbins, C.C.; Cortinas, J.V. Local and synoptic environments associated with freezing rain in the contiguous United States. *Weather Forecast.* **2002**, *17*, 47–65. [[CrossRef](#)]
25. Changnon, S.A. Characteristics of ice storms in the United States. *J. Appl. Meteorol.* **2003**, *42*, 630–639. [[CrossRef](#)]
26. Chen, B.; Hu, W.; Pu, J. Characteristics of the raindrop size distribution for freezing precipitation observed in southern China. *J. Geophys. Res. Atmos.* **2011**, *116*, D06201. [[CrossRef](#)]
27. Zhang, C.y.; Zhang, Y.c. The features of East Asian jet stream in persistent snowstorm and freezing rain processes over southern China in early 2008. *J. Trop. Meteorol.* **2014**, *20*, 349.
28. Kämäräinen, M.; Hyvärinen, O.; Jylha, K.; Vajda, A.; Neiglick, S.; Nuottokari, J.; Gregow, H. A method to estimate freezing rain climatology from ERA-Interim reanalysis over Europe. *Nat. Hazards Earth Syst. Sci.* **2017**, *17*, 243–259. [[CrossRef](#)]
29. Chartrand, J.; Thériault, J.M.; Marinier, S. Freezing rain events that impacted the province of New Brunswick, Canada, and their evolution in a warmer climate. *Atmosphere-Ocean* **2023**, *61*, 40–56. [[CrossRef](#)]
30. McCray, C.D.; Atallah, E.H.; Gyakum, J.R. Long-duration freezing rain events over North America: Regional climatology and thermodynamic evolution. *Weather Forecast.* **2019**, *34*, 665–681. [[CrossRef](#)]
31. Matte, D.; Thériault, J.M.; Laprise, R. Mixed precipitation occurrences over southern Québec, Canada, under warmer climate conditions using a regional climate model. *Clim. Dyn.* **2019**, *53*, 1125–1141. [[CrossRef](#)]
32. Reeves, H.D.; Elmore, K.L.; Ryzhkov, A.; Schuur, T.; Krause, J. Sources of uncertainty in precipitation-type forecasting. *Weather Forecast.* **2014**, *29*, 936–953. [[CrossRef](#)]
33. Cantin, A.; Bachand, D. *Synoptic Pattern Recognition and Partial Thickness Techniques as a Tool for Precipitation Types Forecasting Associated with a Winter Storm*; Service de l'Environnement Atmosphérique, Région du Québec, Centre Météorologique du Québec: Québec, QC, Canada, 1993.
34. Baldwin, M.; Contorno, S. Development of a weather-type prediction system for NMC's mesoscale Eta model. In Proceedings of the 13th Conference on On Weather Analysis And Forecasting, Vienna, VA, USA, 2–6 August 1993.
35. Ramer, J. An empirical technique for diagnosing precipitation type from model output. In Proceedings of the International Conference on Aviation Weather Systems, Vienna, VA, USA, 1–6 August 1993; pp. 227–230.
36. Czys, R.R.; Scott, R.W.; Tang, K.; Przybylinski, R.W.; Sabones, M.E. A physically based, nondimensional parameter for discriminating between locations of freezing rain and ice pellets. *Weather Forecast.* **1996**, *11*, 591–598. [[CrossRef](#)]
37. Bourgooin, P. A method to determine precipitation types. *Weather Forecast.* **2000**, *15*, 583–592. [[CrossRef](#)]
38. Morrison, H.; Grabowski, W.W. A novel approach for representing ice microphysics in models: Description and tests using a kinematic framework. *J. Atmos. Sci.* **2008**, *65*, 1528–1548. [[CrossRef](#)]
39. Ikeda, K.; Steiner, M.; Pinto, J.; Alexander, C. Evaluation of cold-season precipitation forecasts generated by the hourly updating High-Resolution Rapid Refresh model. *Weather Forecast.* **2013**, *28*, 921–939. [[CrossRef](#)]
40. Benjamin, S.G.; Brown, J.M.; Smirnova, T.G. Explicit precipitation-type diagnosis from a model using a mixed-phase bulk cloud-precipitation microphysics parameterization. *Weather Forecast.* **2016**, *31*, 609–619. [[CrossRef](#)]
41. Wandishin, M.S.; Baldwin, M.E.; Mullen, S.L.; Cortinas, J.V. Short-range ensemble forecasts of precipitation type. *Weather Forecast.* **2005**, *20*, 609–626. [[CrossRef](#)]
42. WMO. *Manual on Codes-International Codes, Volume I. 1, Annex II to the WMO Technical Regulations: Part A-Alphanumeric Codes*; WMO: Geneva, Switzerland, 2018.
43. Hersbach, H.; Bell, B.; Berrisford, P.; Hirahara, S.; Horányi, A.; Muñoz-Sabater, J.; Nicolas, J.; Peubey, C.; Radu, R.; Schepers, D.; et al. The ERA5 global reanalysis. *Q. J. R. Meteorol. Soc.* **2020**, *146*, 1999–2049. [[CrossRef](#)]
44. Amjad, M.; Yilmaz, M.T.; Yucel, I.; Yilmaz, K.K. Performance evaluation of satellite-and model-based precipitation products over varying climate and complex topography. *J. Hydrol.* **2020**, *584*, 124707. [[CrossRef](#)]
45. Chen, F.; Liu, Y.; Liu, Q.; Qin, F. A statistical method based on remote sensing for the estimation of air temperature in China. *Int. J. Climatol.* **2015**, *35*, 2131. [[CrossRef](#)]

46. Good, E.J.; Ghent, D.J.; Bulgin, C.E.; Remedios, J.J. A spatiotemporal analysis of the relationship between near-surface air temperature and satellite land surface temperatures using 17 years of data from the ATSR series. *J. Geophys. Res. Atmos.* **2017**, *122*, 9185–9210. [[CrossRef](#)]
47. Birk, K.; Lenning, E.; Donofrio, K.; Friedlein, M.T. A revised Bourgouin precipitation-type algorithm. *Weather Forecast.* **2021**, *36*, 425–438. [[CrossRef](#)]
48. Aburomman, A.A.; Reaz, M.B.I. A survey of intrusion detection systems based on ensemble and hybrid classifiers. *Comput. Secur.* **2017**, *65*, 135–152. [[CrossRef](#)]
49. Sultan Zia, M.; Hussain, M.; Arfan Jaffar, M. A novel spontaneous facial expression recognition using dynamically weighted majority voting based ensemble classifier. *Multimed. Tools Appl.* **2018**, *77*, 25537–25567. [[CrossRef](#)]
50. Dogan, A.; Birant, D. A weighted majority voting ensemble approach for classification. In Proceedings of the 2019 4th International Conference on Computer Science and Engineering (UBMK), Samsun, Turkey, 11–15 September 2019; pp. 1–6.
51. Rojarath, A.; Songpan, W.; Pong-inwong, C. Improved ensemble learning for classification techniques based on majority voting. In Proceedings of the 2016 7th IEEE International Conference on Software Engineering and Service Science (ICSESS), Beijing, China, 26–28 August 2016; pp. 107–110.
52. Zerr, R.J. Freezing rain: An observational and theoretical study. *J. Appl. Meteorol.* **1997**, *36*, 1647–1661. [[CrossRef](#)]
53. Bernstein, B.C. Regional and local influences on freezing drizzle, freezing rain, and ice pellet events. *Weather Forecast.* **2000**, *15*, 485–508. [[CrossRef](#)]
54. Carrière, J.M.; Lainard, C.; Le Bot, C.; Robart, F. A climatological study of surface freezing precipitation in Europe. *Meteorol. Appl.* **2000**, *7*, 229–238. [[CrossRef](#)]
55. Roberts, E.; Stewart, R.E. On the occurrence of freezing rain and ice pellets over the eastern Canadian Arctic. *Atmos. Res.* **2008**, *89*, 93–109. [[CrossRef](#)]
56. Roebber, P.J. Visualizing multiple measures of forecast quality. *Weather Forecast.* **2009**, *24*, 601–608. [[CrossRef](#)]
57. Heidke, P. Berechnung des Erfolges und der Güte der Windstärkevorhersagen im Sturmwarnungsdienst. *Geogr. Ann.* **1926**, *8*, 301–349.
58. Jolliffe, I.T.; Stephenson, D.B. *Forecast Verification: A Practitioner's Guide in Atmospheric Science*; John Wiley & Sons: Hoboken, NJ, USA, 2012.
59. Lei, H.; Zhao, H.; Ao, T. A two-step merging strategy for incorporating multi-source precipitation products and gauge observations using machine learning classification and regression over China. *Hydrol. Earth Syst. Sci.* **2022**, *26*, 2969–2995. [[CrossRef](#)]
60. Sohn, K.T.; Lee, J.H.; Lee, S.H.; Ryu, C.S. Statistical prediction of heavy rain in South Korea. *Adv. Atmos. Sci.* **2005**, *22*, 703–710. [[CrossRef](#)]

Disclaimer/Publisher's Note: The statements, opinions and data contained in all publications are solely those of the individual author(s) and contributor(s) and not of MDPI and/or the editor(s). MDPI and/or the editor(s) disclaim responsibility for any injury to people or property resulting from any ideas, methods, instructions or products referred to in the content.